JACS Au
AN OPEN ACCESS JOURNAL OF THE AMERICAN CHEMICAL SOCIETY

pubs.acs.org/jacsau
Article

Multiple Interlayer Interactions Enable Highly Stable X-ray Detection in 2D Hybrid Perovskites

Haiqing Zhong, Shihai You,* Jianbo Wu, Zeng-Kui Zhu, Panpan Yu, Hang Li, Zi-Yang Wu, Yang Li, Qianwen Guan, Hongliang Dai, Chang Qu, Jiahong Wang, Shuang Chen, Chengmin Ji, and Junhua Luo*

Cite This: JACS Au 2024, 4, 2393−2402

ABSTRACT: Metal halide perovskites have outperformed conventional inorganic semiconductors in direct X-ray detection due to their ease of synthesis and intriguing photoelectric properties. However, the operational instability caused by severe ion migration under a high external electric field is still a big concern for the practical application of perovskite detectors. Here, we report a 2D $(BPEA)_2PbI_4$ (BPEA = *R*-1-(4-bromophenyl)ethylammonium) perovskite with Br-substituted aromatic spacer capable of introducing abundant interactions, e.g., the molecular electrostatic forces between Br atoms and aromatic rings and halogen bonds of Br−I, in the interlayer space, which effectively suppresses ion migration and thus enables superior operational stability. Constructing direct X-ray detectors based on high-quality single crystals of $(BPEA)_2PbI_4$ results in a high sensitivity of 1,003 μC Gy^{-1} cm^{-2}, a low detection limit of 366 nGy s^{-1}, and an ultralow baseline drift of 3.48 × 10^{-8} nA cm^{-1} s^{-1} V^{-1} at 80 V bias. More strikingly, it also exhibits exceptional operational stability under high flux, long-time X-ray irradiation, and large working voltage. This work shows an integration of multiple interlayer interactions to stabilize perovskite X-ray detectors, providing new insights into the future design of perovskite optoelectronic devices toward practical application.

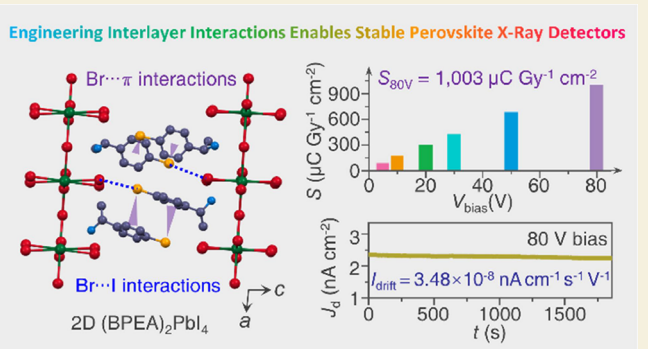

KEYWORDS: *2D perovskite, X-ray detection, interlayer interaction, operational stability, ion migration, single crystal*

INTRODUCTION

X-rays with strong penetrating capability have been widely applied to many essential fields, such as medical imaging, security screening, and nondestructive product tests.[1−4] As a key component of X-ray detectors, X-ray sensitive materials directly determine device performance, thus driving ongoing explorations on high-performance X-ray detection materials.[5−11] In recent years, benefiting from the solution-processed synthesis, exceptional photoelectric properties, and strong X-ray attenuation, lead halide perovskites (LHPs) have achieved significant advances in X-ray detection.[12−21] In 2015, 3D $MAPbI_3$ (MA = methylamine) was first used for direct X-ray detection, obtaining a sensitivity (S) of 25 μC Gy^{-1} cm^{-2}, which arouses explosive research on LHP-based X-ray detectors.[12] To date, an ultrahigh sensitivity of 2.2 × 10^8 μC Gy^{-1} cm^{-2} and an extremely low detection limit (LoD) of 0.1 nGy s^{-1} have been achieved in $MAPbI_3$-based direct X-ray detectors,[19,20] far surpassing conventional X-ray detection semiconductors such as Si, HgI_2, and α-Se. Despite these great achievements, the severe ion migration (e.g., halogen ions) in 3D LHPs under high working voltages, causing large dark current and current noise as well as serious baseline drift (about 10^{-3} nA cm^{-1} s^{-1} V^{-1}), are still severely limiting their detection performance and operational stability improvement.[10,21,22]

In contrast, 2D LHPs with alternating inorganic perovskite slabs and organic spacer layers structure naturally provide resistive organic barriers to inhibit ion migration, reduce dark current, and improve structural stability, therefore giving them great potential for fabricating operationally stable optoelectronic devices, including stable X-ray detectors.[23−26] For example, a small dark current drift (I_{drift}) of 7.76 × 10^{-6} nA cm^{-1} s^{-1} V^{-1} has been achieved in a direct X-ray detector based on 2D $(2IPA)_2(FA)Pb_2I_7$ (2IPA = 2-iodopropylammonium, FA = formamidine) perovskite single crystal (SC), which is about 1000 folds lower than its 3D counterparts, exhibiting superior operational stability.[27] More recently, to further improve the operating stability of 2D LHP devices, some researchers have focused on strengthening interlayer inter-

Received: April 20, 2024
Revised: May 16, 2024
Accepted: May 21, 2024
Published: June 10, 2024

https://doi.org/10.1021/jacsau.4c00345
JACS Au 2024, 4, 2393−2402

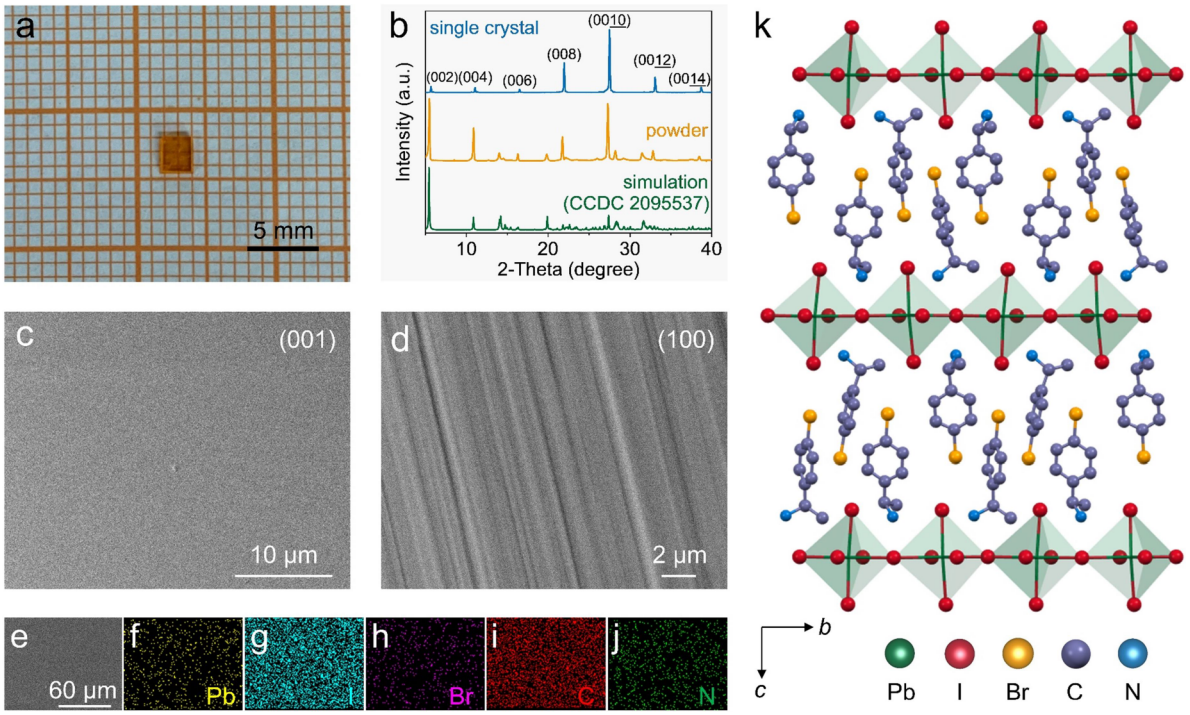

Figure 1. Crystal structure and micromorphology. (a) Photograph of a bulk SC of $(BPEA)_2PbI_4$. (b) PXRD patterns of $(BPEA)_2PbI_4$ powders and SC. (c,d) SEM images of (001) and (100) crystallographic planes of $(BPEA)_2PbI_4$ SC, respectively. (e–j) SEM image of a selected area in $(BPEA)_2PbI_4$ SC and corresponding elemental mappings. (k) Crystal structure of $(BPEA)_2PbI_4$ viewed along the *a*-axis. H atoms have been omitted for the sake of clarity.

actions among adjacent inorganic perovskite sheets, and remarkable success has been achieved.[28−34] Ren and co-workers constructed a novel 2D Ruddlesden−Popper (RP) phase perovskite, $(2\text{-(methylthio)ethylamine})_2(MA)_4Pb_5I_{16}$, that successfully creates strong sulfur−sulfur interactions in the organic bilayers, thus allowing for the fabrication of a highly stable and efficient solar cell.[28] Fu et al. found that establishing strong and homogeneous halogen bonds (I−I bonds) between organic spacer layers and inorganic perovskite slabs in $(1\text{-(4-iodophenyl)ethanamine})_2PbI_4$ can effectively block halogen ion migration routes.[29] Benefiting from such a blocking effect, a very stable red perovskite light-emitting diode with an operational half-life of ∼540 min is successfully constructed. Inspired by these exciting results, we plan to strengthen the interlayer interactions in 2D LHPs by purposely designing their spacers, reducing ion migration under large external electric fields, and finally realizing stable X-ray detection.

In this work, we present an ultrastable direct X-ray detector based on a 2D RP-type perovskite $(BPEA)_2PbI_4$ (BPEA = *R*-1-(4-bromophenyl)ethylammonium) with a Br-substituted aromatic spacer. The elaborately introduced Br atoms not only form abundant molecular electrostatic interactions with adjacent benzene rings (Br···π) but also interact with I atoms in the perovskite skeleton to form strong halogen bonds (Br−I), which synergistically blocks paths for ion migration, thus enabling high operational stability. High-quality SCs of $(BPEA)_2PbI_4$ were grown via a facile solution process, which exhibits a high bulk resistivity of 1.46×10^{11} Ω cm, a large mobility-lifetime product ($\mu\tau$) of 3.26×10^{-4} cm^2 V^{-1}, and excellent photoresponse under visible light illumination. Combining the efficient X-ray absorption, outstanding optoelectronic performance, and most importantly, strong interlayer interactions in $(BPEA)_2PbI_4$, a highly stable perovskite X-ray detector is successfully fabricated, possessing a high sensitivity of 1,003 μC Gy^{-1} cm^{-2}, a low LoD of 366 nGy s^{-1}, as well as an extremely small I_{drift} of 3.48×10^{-8} nA cm^{-1} s^{-1} V^{-1}. More intriguingly, the superior operational stability of this detector is also realized even under long-time, high-flux X-ray irradiation and a large working voltage.

RESULTS AND DISCUSSION

Crystal Growth and Micromorphology

Bulk SCs of $(BPEA)_2PbI_4$ with an orange color and a size up to $2.5 \times 2.5 \times 0.4$ mm^3 were grown from a hot hydroiodic acid solution containing stoichiometric starting chemicals via a gradual temperature-cooling process (Figure 1a). Their phase purity is verified by the powder X-ray diffraction (PXRD) patterns, as shown in Figure 1b, in which the diffraction peaks match well with those in the simulated PXRD pattern (CCDC 2095537).[35] The XRD scan of a $(BPEA)_2PbI_4$ SC surface shows intense and sharp diffraction peaks of the (00*l*) crystallographic planes (*l* = 2, 4, 6, 8, 10, 12, and 14), revealing its well-oriented growth and good crystallinity (Figure 1b). Figure S1 presents the PXRD patterns of $(BPEA)_2PbI_4$ fresh and after exposure to air for 90 days, which show no phase change, indicating its excellent environmental stability. The thermogravimetric (TG) curve plotted in Figure S2 shows that $(BPEA)_2PbI_4$ has good thermal stability, with a high decomposition temperature of up to 252 °C in a N_2 atmosphere. Figure 1c presents the scanning electron microscope (SEM) images of the (001) plane of a $(BPEA)_2PbI_4$ SC, which appears to be very smooth and free of defects. The SEM image of the (100) plane displays periodically spaced layers (Figure 1d), suggesting the strong

https://doi.org/10.1021/jacsau.4c00345
JACS Au 2024, 4, 2393−2402

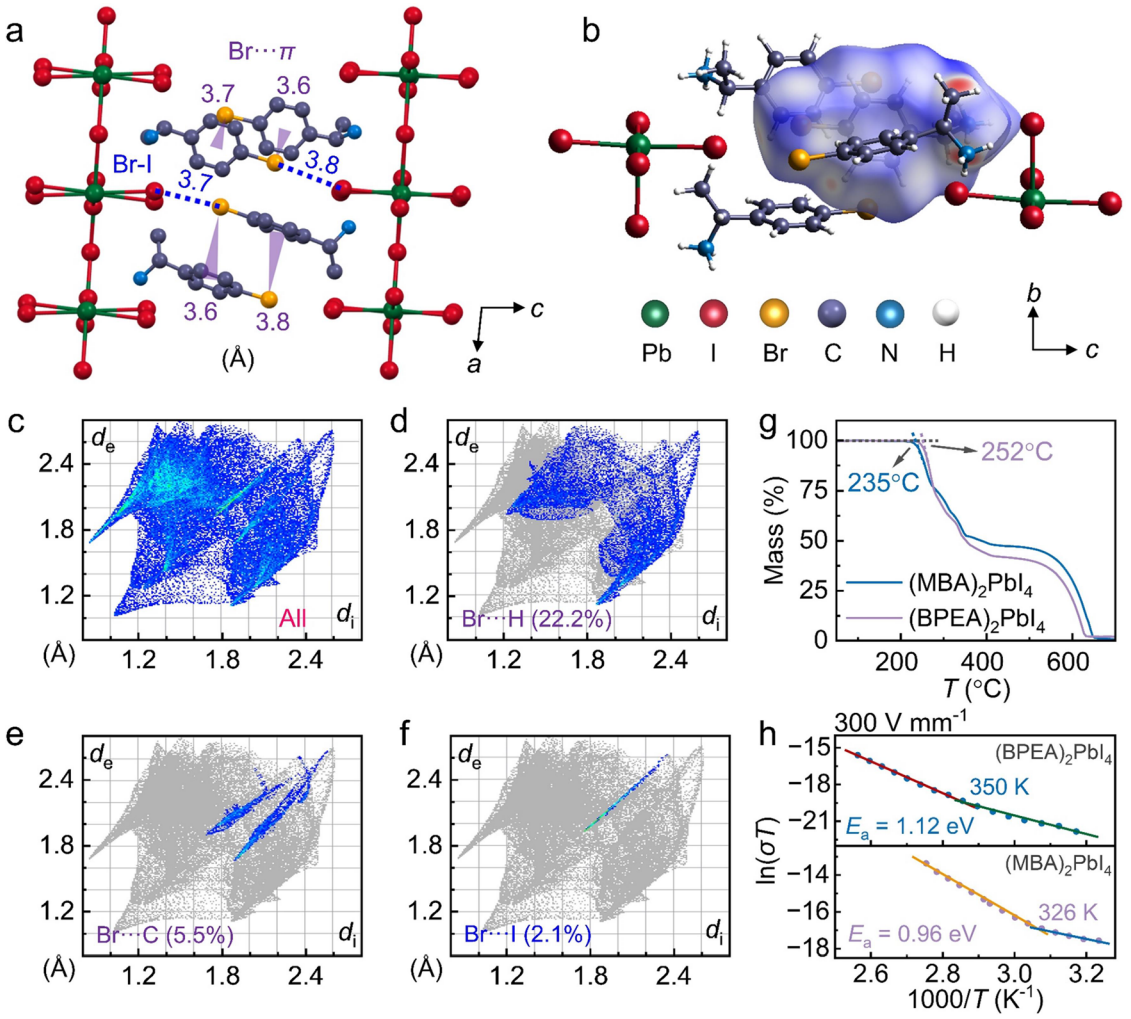

Figure 2. Molecular interactions. (a) Distances for Br atoms to adjacent I atoms and neighbor benzene rings, respectively, in $(BPEA)_2PbI_4$ structure. H atoms are omitted for clarity. (b) Hirshfeld surface of BPEA cation and (c–f) corresponding 2D fingerprint mappings for all Br···H, Br···C, and Br···I contacts in the asymmetric unit of $(BPEA)_2PbI_4$. The red spots on Hirshfeld surface in (b) represent the distance between two atoms less than the sum of van der Waals radii, indicating shorter contact. (g) TG curves of $(MBA)_2PbI_4$ and $(BPEA)_2PbI_4$, respectively. (h) Temperature-dependent conductivity of $(BPEA)_2PbI_4$ and $(MBA)_2PbI_4$ SCs measured at an electric field of 300 V mm^{-1}.

parallel growth habit of $(BPEA)_2PbI_4$, which agrees with the previous observation for 2D layered LHPs. The X-ray energy dispersive spectroscopy (EDS) mappings of a selected SC are demonstrated in Figure 1e–j, demonstrating that Pb, I, Br, C, and N elements are uniformly distributed within the crystal. To further evaluate the quality of the $(BPEA)_2PbI_4$ SC, the space-charge-limited current (SCLC) method was adopted to measure its trap density (n_{trap}). As shown in Figure S3, the Ohmic region ($n = 1$) and the trap filling limited (TFL) region ($n > 3$) are observed in the logarithmic current–voltage (I–V) curve. From which, the n_{trap} value is determined to be 2.08×10^9 cm^{-3}, which is lower than some similar 2D hybrid perovskite SCs, e.g., $(PEA)_2PbI_4$ (PEA = phenethylamine, 3.71×10^{10} cm^{-3}) and $(4\text{-F-PEA})_2PbI_4$ (4-F-PEA = 4-fluorophenethylammonium, 6.24×10^9 cm^{-3}),[30,32] suggesting its high crystal quality. Figure 1k depicts the crystal structure of $(BPEA)_2PbI_4$, adopting a pure 2D RP motif. The $[PbI_6]^{4-}$ octahedra are corner-connected to form monolayered inorganic slabs, which further alternate with the bilayered organic spacers of BPEA.

Interlayer Interactions

To gain deeper insights into the effect of this halogen-substituted aromatic spacer, we further analyze molecular interactions in the interlayer space of the $(BPEA)_2PbI_4$ structure. As shown in Figure S4, these organic BPEA cations are firmly anchored to inorganic slabs by strong N–H···I hydrogen bonds. Normally, in the organic bilayers of 2D RP-type perovskites, there only exists relatively weak van der Waals forces, however, in this compound with Br-substituted aromatic cations, it is expected to form additional molecular electrostatic forces due to the short distance between Br atoms and the adjacent benzene rings (e.g., 3.6 Å), as shown in Figure 2a.[32,33,36] Indeed, as displayed in the Hirschfeld surface analysis (Figures 2b–e and S5),[37] strong molecular electrostatic interactions between electron-deficient Br atoms and electron-rich benzene rings (Br···π) are observed, which strengthen the link among organic spacers. Such a strong interaction between halogen atoms and neighboring benzene rings (e.g., F···π) has also been reported in a similar compound $(4\text{-F-PEA})_2PbI_4$.[32] Moreover, the shortest distance between Br atoms on organic cations and I atoms in inorganic $[PbI_4]^{2-}$ sheet is measured to be 3.7 Å (Figure 2a), which is smaller

https://doi.org/10.1021/jacsau.4c00345
JACS Au 2024, 4, 2393–2402

than the sum of two atomic radii for interacting (e.g., $r_{Br} + r_I$ = 3.8 Å),[29] thus allowing the formation of Br−I halogen bonds (Figure 2b, f). It should be noted that not all 2D hybrid perovskites with halogen-substituted spacers can form halogen bonds between the halogen atoms on organic ligands and the halogen atoms in an inorganic framework because their distance often is greater than the sum of van der Waals radii (Table S1). Thus, introducing proper halogenated organic ligands is crucial. Both the halogen···π interactions and halogen bonds have been solidly proven to be beneficial to blocking ion migration paths and thus stabilizing crystal structure in 2D halide perovskites, which further contributes to improving operational stability of their optoelectronic devices, for instance, perovskite LEDs.[29,33,38] This is also supported by the enhanced thermal stability of $(BPEA)_2PbI_4$ compared to a highly similar compound of $(MBA)_2PbI_4$ (MBA = methylbenzylammonium) just without Br substitution on organic spacers (Figures 2g and S6).[32] To further understand the effect of these interlayer interactions on suppressing ion migration, the activation energy (E_a) for ion migration of $(BPEA)_2PbI_4$ and $(MBA)_2PbI_4$ SCs was calculated from its temperature-dependent conductivity curve according to the Nernst−Einstein equation,[39,40]

$$\sigma(T) = \left(\frac{\sigma_0}{T}\right)\exp\left(\frac{-E_a}{k_B T}\right) \quad (1)$$

where σ is the conductivity at a given temperature T, σ_0 is a constant, and k_B is the Boltzmann's constant (8.617×10^{-5} eV K^{-1}). By fitting the correlation between $\ln(\sigma T)$ and $1000/T$ (Figure 2h), it is clear that there exists a transition from electronic to ionic conductivity in both compounds when the temperature increases. The fitting result shows that E_a (1.12 eV) for $(BPEA)_2PbI_4$ is larger than that of $(MBA)_2PbI_4$ (E_a = 0.96 eV), which can be ascribed to the contribution of Br atoms on organic cations. Moreover, this activation energy of $(BPEA)_2PbI_4$ is also much higher than those of 3D LHP SCs, i.e., $MAPbI_3$ (276 K, E_a = 0.624 eV),[40] and many 2D hybrid perovskites, such as $(4\text{-F-PEA})_2PbI_4$ (331 K, E_a = 0.87 eV),[33] (1,4-butanediammonium)PbI_4 (375 K, E_a = 0.88 eV),[39] and $(NH_4)_3Bi_2I_9$ (350 K, E_a = 0.91 eV),[9] which suggests that strong interlayer interactions are beneficial to increasing the energy barrier for ion migration, eventually inhibiting ion migration. In this context, we think that the abundant interlayer forces (e.g, Br···π and Br−I interactions) in $(BPEA)_2PbI_4$ induced by halogen-substituted aromatic ligands are expected to realize direct X-ray detection with improved operational stability.

Semiconducting Characteristics

The absorption spectrum of $(BPEA)_2PbI_4$ powders is recorded on an ultraviolet−visible-near-infrared spectrometer to estimate its optical band gap (E_g). As plotted in Figure 3a, $(BPEA)_2PbI_4$ presents an absorption cutoff at around 546 nm, from which its E_g is derived to be 2.31 eV according to the Tauc's plot.[41] This value is in good agreement with the previously reported result (2.34 eV).[35] Figure S7 presents the bulk resistivity (ρ) of a $(BPEA)_2PbI_4$ SC along the inorganic plane. It is measured to be 1.46×10^{11} Ω cm, comparable to the values of some reported 2D perovskite SCs, e.g., $(PEA)_2PbI_4$ (1.07×10^{11} Ω cm),[30] $(o\text{-F-PEA})_2PbI_4$ (4.8×10^{11} Ω cm, o-F-PEA = orth-fluorophenethylammine),[30] and $(4AEPy)PbI_4$ (2.86×10^{11} Ω cm, 4AEPy = 4-(2-aminoethyl)-pyridine)[34] but is about 1,000 times higher than those of 3D

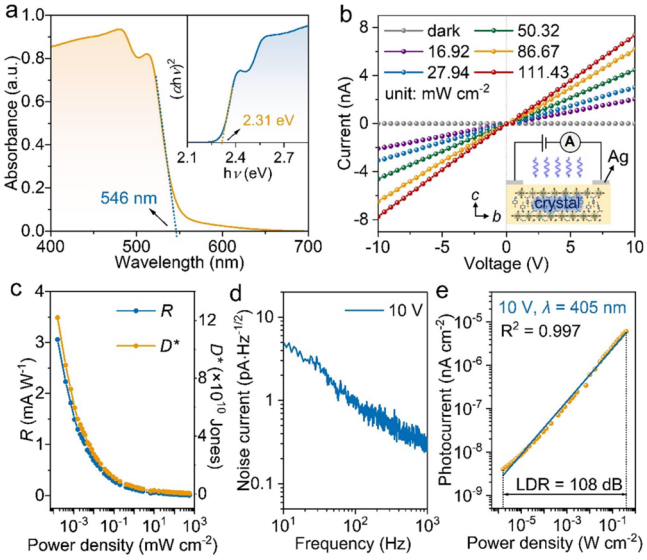

Figure 3. Semiconducting properties. (a) UV-*vis* absorption spectrum of $(BPEA)_2PbI_4$ powder, showing a cutoff at 546 nm. The inset is derived optical band gap (2.31 eV). (b) $I-V$ traces of $(BPEA)_2PbI_4$ SC device in the dark and under 405 nm illumination. The inset is the corresponding device structure. (c) R and D^* values of $(BPEA)_2PbI_4$ device under 405 nm light illumination at 10 V bias. (d) Noise current spectrum measured from 10 to 1000 Hz at 10 V bias. (e) LDR of $(BPEA)_2PbI_4$ detector with incident light intensity ranging from 1.58 $\times 10^{-3}$ to 400 mW cm^{-2} at 10 V.

LHP SCs (10^7-10^8 Ω cm).[42] Such a large bulk resistivity is advantageous for minimizing dark current and noise current, thereby contributing to achieving high-performance X-ray detection.[8]

The photoelectric performance of $(BPEA)_2PbI_4$ SC under visible light illumination is evaluated by adopting a two-terminal planar device structure, Ag/$(BPEA)_2PbI_4$ SC/Ag (the inset of Figures 3b and S8). Figures 3b and S9 plot the $I-V$ traces of the SC device in dark and under 405 nm laser illumination, which shows perfect symmetric and linear correlations, suggesting a good Ohmic contact with a low contact resistance between SC and Ag electrodes is formed.[27,43] Notably, a low dark current (I_d) of 4.91 pA at 10 V bias is obtained, which reveals the low intrinsic carrier concentration and high quality of the $(BPEA)_2PbI_4$ SCs. Under 405 nm laser illumination, the photocurrent (I_{ph}) rises sharply with increased light power density, which can be ascribed to the increased carrier concentration induced by the photoelectric effect. Specifically, I_{ph} can reach 7.35 nA at a 10 V bias under a light power density of 111.43 mW cm^{-2}. Such a quite low I_d coupled with a high I_{ph} thus generates a light on/off ratio of 1.50×10^3, suggesting the excellent optoelectronic performance of $(BPEA)_2PbI_4$ SCs. The current−time ($I-t$) curves upon light on/off switching are presented in Figure S10, which shows stable and repeatable photoresponse, further confirming the reliable optoelectronic performance of the $(BPEA)_2PbI_4$ SC device. To further assess the detection performance of $(BPEA)_2PbI_4$ SC device, the responsivity (R) and detectivity (D^*) are introduced, which can be calculated by,[44]

$$R = (I_{ph} - I_d)/(PA) \quad (2)$$

$$D^* = R/(2eI_d/A)^{1/2} \quad (3)$$

https://doi.org/10.1021/jacsau.4c00345
JACS Au 2024, 4, 2393−2402

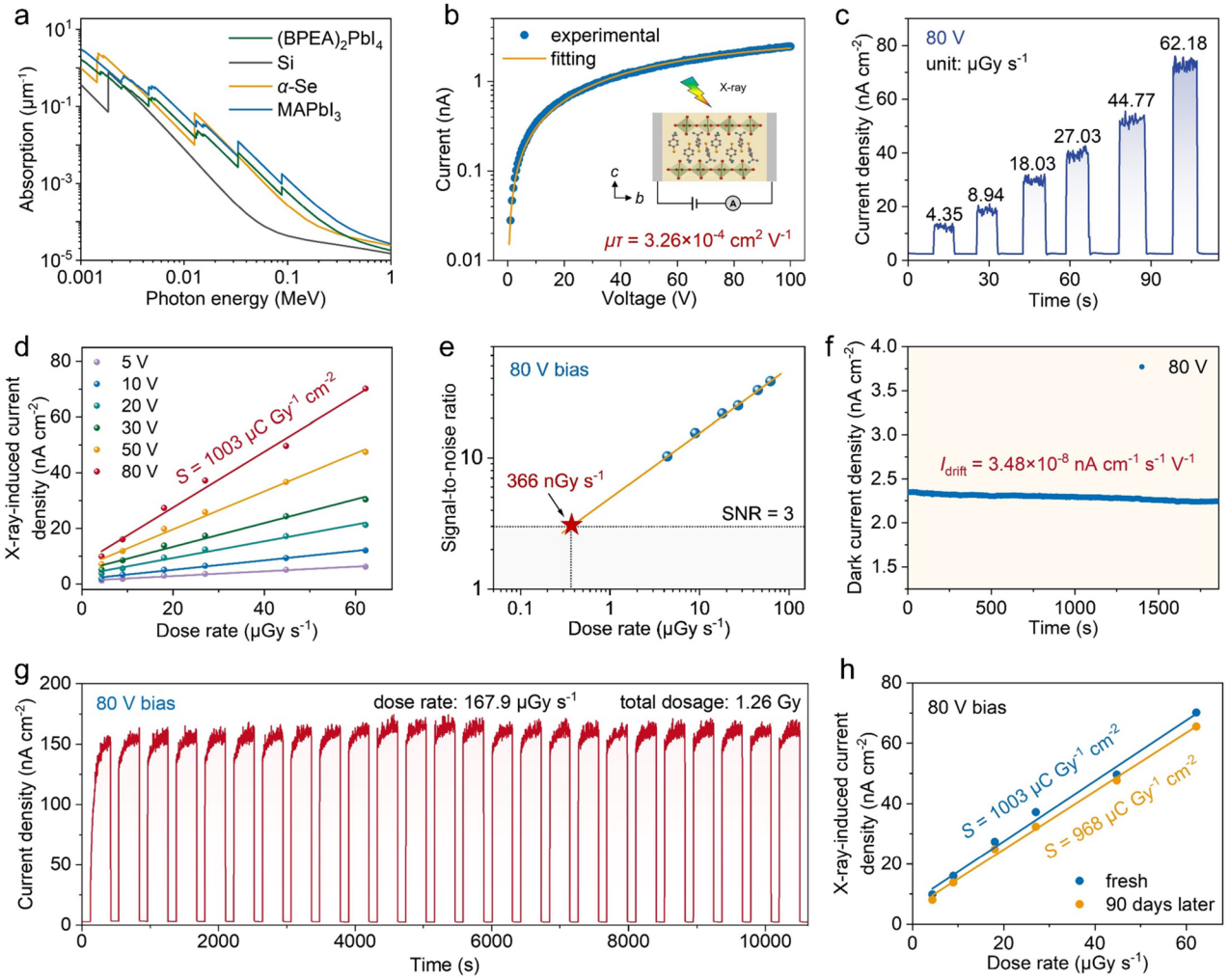

Figure 4. X-ray detection performance. (a) Absorption coefficients of $(BPEA)_2PbI_4$, Si, α-Se, and $MAPbI_3$ as a function of photon energies. (b) Voltage-dependent photocurrent of $(BPEA)_2PbI_4$ SC under X-ray irradiation along the inorganic layer, deriving a $\mu\tau$ value of 1.13×10^{-4} cm^2 V^{-1}. The inset shows the schematic device. (c) $I-t$ curves of the $(BPEA)_2PbI_4$ device under X-ray irradiation with increased dose rate at an 80 V bias voltage. (d) X-ray-induced current density as a function of dose rate at various bias voltages (e.g., 5, 10, 20, 30, 50, and 80 V). Fitting their slopes gives the sensitivity of the $(BPEA)_2PbI_4$ detector. (e) SNR versus X-ray dose rate at 80 V bias for the SC detector, from which derives the detection limit at 366 nGy s^{-1}. (f) Dark current shift of the $(BPEA)_2PbI_4$ detector at 80 V bias. (g) Device operational stability under continuous X-ray irradiation of a high dose rate of 167.9 μGy s^{-1} and a large bias voltage of 80 V. (h) X-ray-induced current density versus dose rate of $(BPEA)_2PbI_4$ device at fresh and after exposure to ambient air for 90 days, showing exceptional environmental stability.

in which P is the light power density, A is the effective illumination area, and e is the unit charge. As shown in Figure 3c, R and D^* gradually decrease with increasing light power density, and the maximum values are estimated to be 3.06 mA W^{-1} and 1.22×10^{11} Jones under 158 nW cm^{-2} illumination at 10 V bias, respectively. They are comparable to previously reported results.[35] Due to the noise current being an important figure of merit of photodetectors, the dark noise current (i_n) of $(BPEA)_2PbI_4$ SC device under a 10 V bias is also measured (Figure 3d), in which the i_n value at 50 Hz is determined to be 1.73×10^{-12} A Hz$^{-1/2}$. Then, the D^* can also be estimated according to $D^* = R(Af)^{1/2}/i_n$, where f is the bandwidth.[45] Figure S11 shows the comparison of D^* calculated from the dark current and the noise current. The maximum D^* value based on the noise current is determined to be 7.74×10^8 Jones at 158 nW cm^{-2}, which is more than 2 orders of magnitude lower than that calculated from the dark current. To figure out the linear dynamic range (LDR) of this device, the correlation between the photocurrent and the light power densities from around 1.58×10^{-3} to 400 mW cm^{-2} is given in Figure 3e, yielding a large LDR of 108 dB according to LDR = 20 log(P_{max}/P_{min}), where P_{max} (P_{min}) is the maximum (minimum) light power density in the linear range.[46]

X-ray Detection

Considering the outstanding optoelectronic performance of $(BPEA)_2PbI_4$, we further fabricated it into SC devices for detecting X-rays. To exploit the better carrier transport along the in-plane direction of 2D perovskite and effectively collect carriers induced by X-rays within the crystal, a two-terminal bulk device structure (Ag/$(BPEA)_2PbI_4$ SC/Ag) by depositing Ag electrodes on two sides of the crystal along the b-axis was adopted (Figure S12). First, the absorption coefficients over a broad photon energy (1−1000 keV) for $(BPEA)_2PbI_4$ and some representative X-ray detection materials, such as Si, α-Se, and $MAPbI_3$, are calculated based on NIST's photon cross-section database.[47] As plotted in Figure 4a, the linear absorption coefficient of $(BPEA)_2PbI_4$ is significantly higher than that of Si and approaches that of $MAPbI_3$, revealing its

https://doi.org/10.1021/jacsau.4c00345
JACS Au 2024, 4, 2393−2402

good X-ray attenuation across the entire energy range. The attenuation efficiencies of these materials as a function of thickness for 50 keV (the maximum energy of our X-ray source) X-ray photons are given in Figure S13. It is clear that $(BPEA)_2PbI_4$ has a higher attenuation efficiency than that of conventional Si and α-Se. At a thickness of 1 mm, the $(BPEA)_2PbI_4$ SC can absorb 89% of the incident X-ray photons, which is comparable to that of the $MAPbI_3$ SC (98%). Such a strong attenuation can ensure the adequate absorption of X-rays even at a relatively thin SC thickness. The charge collection plays another vital role in direct X-ray detection, which can be assessed by the $\mu\tau$ product. A high $\mu\tau$ value is preferred for fabricating high-performance X-ray detectors. Here, the $\mu\tau$ value is derived by fitting the voltage-dependent photocurrent of $(BPEA)_2PbI_4$ SC under X-ray irradiation according to the Hecht equation,[3,17]

$$I = \frac{I_0 \mu\tau V}{L^2}\left[1 - \exp\left(-\frac{L^2}{\mu\tau V}\right)\right] \quad (4)$$

where I is the photocurrent, I_0 is the saturated photocurrent, V is the bias voltage, *and* L represents the electrode spacing. As given in Figure 4b, the $\mu\tau$ value for $(BPEA)_2PbI_4$ SC along the in-plane direction is 3.26×10^{-4} cm^2 V^{-1}, comparable to some reported 2D monolayered LHP SCs, like $(PEA)_2PbI_4$ (1.07×10^{-4} cm^2 V^{-1}),[30] $(4\text{-F-PEA})_2PbI_4$ (5.1×10^{-4} cm^2 V^{-1}),[32] and $(4AEPy)PbI_4$ (3.57×10^{-4} cm^2 V^{-1}),[34] but is much higher than that of commercial α-Se film (about 10^{-7} cm^2 V^{-1}).[3] Figure S14 shows the value of the out-of-plane direction in 2D perovskite SC (1.03×10^{-4} cm^2 V^{-1}), which is about 3 times lower than that of the in-plane direction, evidencing its inferior carrier transport. Owing to such integration of efficient X-ray absorption, high $\mu\tau$ product along the in-plane direction, strong interlayer interaction, low dark current, excellent optoelectronic performance, and good environmental stability in $(BPEA)_2PbI_4$, we believe that it is a highly promising candidate for high-performance X-ray detectors.

Figure S15 shows the $I-V$ traces of the $(BPEA)_2PbI_4$ SC detector in the dark and under X-ray irradiation with various dose rates, which first demonstrates its effective X-ray response performance. A high sensitivity and low LoD are two key parameters for a practical X-ray detector. The sensitivity of a photoconductive X-ray detector is defined as the collected charge density per unit of radiation exposure, which can be calculated using the following formula,[8]

$$S = (J_{ph} - J_d)/D \quad (5)$$

in which J_d and J_{ph} are current densities in the dark and under X-ray irradiation, respectively, and D is the X-ray dose rate. To evaluate the sensitivity of our detector, $J-t$ curves under different bias voltages (e.g., 5, 10, 20, 30, 50, and 80 V) and various X-ray dose rates are measured, as shown in Figures 4c and S16. Notably, a highly stable baseline is obtained in this device even at a large working voltage of 80 V, which is different from the serious baseline drift in 3D LHPs, revealing excellent working stability. By gradually increasing X-ray dose rate, J_{ph} shows a remarkable growth under all bias voltages, indicating the outstanding X-ray photoresponse of $(BPEA)_2PbI_4$. Specifically, a large photocurrent density of 72.67 nA cm^{-2} under 62.18 μGy s^{-1} and 80 V bias is obtained, which is much higher than that at 5 V bias under a same dose rate (6.46 nA cm^{-2}), due to the more efficient charge collection under large external electric field.[8,13] By linearly fitting the correlation between the X-ray-generated current density ($J_{ph} - J_d$) and dose rate, the sensitivities at different bias voltages are obtained (Figure 4d). As presented in Figure S17, the sensitivity gradually increases with the increasing bias voltage, reaching a maximum of 1003 μC Gy^{-1} cm^{-2} at 80 V bias. This value is comparable to many reported X-ray detectors based on 2D LHP SCs, such as $(4\text{-F-PEA})_2PbI_4$ (3402 μC Gy^{-1} cm^{-2} @ 200 V),[32] $(PEA)_2PbI_4$ (848 μC Gy^{-1} cm^{-2} @ 1250 V mm^{-1}),[30] and $(2IPA)_2(FA)Pb_2I_7$ (438 μC Gy^{-1} cm^{-2} @ 10 V),[27] but it is more than 50 times higher than that of the commercial α-Se film detector operated under an ultrahigh electric field of 10,000 V mm^{-1} (20 μC Gy^{-1} cm^{-2}),[14] as listed in Table S2. Such a high sensitivity evidence of the high X-ray detection performance of $(BPEA)_2PbI_4$. Furthermore, the LoD is determined by calculating the signal-to-noise ratio (SNR).[8,9] According to the definition provided by the International Union of Pure and Applied Chemistry, the dose rate with an SNR = 3 is the LoD of an X-ray detector.[8] SNRs under various X-ray dose rates at 80 V bias are displayed in Figure 4e. It shows that a high SNR of about 10 is obtained at a low dose rate of 4.35 μGy s^{-1}. Further fitting the relationship between SNR and dose rate, a LoD of 366 nGy s^{-1} is estimated. Such a low LoD is about 15 folds lower than that required for regular medical imaging (5.5 μGy s^{-1}).[9,14] Hence, it is beneficial to reduce the radiation risk.

The device stability is another key performance indicator for X-ray detectors. To quantify this performance, the I_{drift} is introduced, which can be computed by the following formula,[6,48]

$$I_{drift} = (I_t - I_{initial})/(E \times A \times t) \quad (6)$$

where $I_{initial}$ and I_t are dark currents at initial and time t, respectively, A is the device area, and E is the electric field. As presented in Figure 4f, an extremely small I_{drift} of 3.48×10^{-8} nA cm^{-1} s^{-1} V^{-1} is obtained under 80 V bias voltage, which not only 5 orders of magnitude lower than that in 3D LHP detectors (about 10^{-3} nA cm^{-1} s^{-1} V^{-1}) but also outperforms those stable 2D LHP X-ray detectors reported recently, such as $(PEA)PbBr_4$ (6.2×10^{-6} nA cm^{-1} s^{-1} V^{-1}),[10] $(PEA)_2PbI_4$ (1.9×10^{-7} nA cm^{-1} s^{-1} V^{-1}),[10] $(DGA)PbI_4$ (DGA = dimethybiguanide, 5.97×10^{-7} nA cm^{-1} s^{-1} V^{-1}),[31] and $(4\text{-F-PEA})_2PbI_4$ (4.9×10^{-8} nA cm^{-1} s^{-1} V^{-1}),[32] as listed in Table S2, highlighting its exceptional operating stability. Such a low I_{drift} can be ascribed to the effectively suppressed ion migration resulting from the strong interlayer interactions (e.g., Br$\cdots\pi$ and Br–I bonds) in $(BPEA)_2PbI_4$. Furtherly, the operational stability of this device has also been assessed by exposing it to continuous, long-time X-ray irradiation of high dose rate (167.9 μGy s^{-1}) at a large working voltage of 80 V. Notably, a highly stable and repeatable baseline and photocurrent is observed (Figure 4g), which reveals the great promise of $(BPEA)_2PbI_4$ SC detector for practical application. Moreover, after exposure to ambient air (RH 45% and 25 °C) for 90 days, there is no significant degradation in photoresponse to X-rays (Figure 4h), thus highlighting the excellent environmental stability of the $(BPEA)_2PbI_4$ SC device. Such excellent environmental stability is comparable with other 2D perovskite with halogenated aromatic ligands, like $(4\text{-F-PEA})_2PbI_4$,[32] which can be ascribed to the stabilization effect of multiple interlayer interactions on 2D perovskite phases.

https://doi.org/10.1021/jacsau.4c00345
JACS Au 2024, 4, 2393–2402

CONCLUSIONS

In summary, we report an ultrastable X-ray detector-based 2D $(BPEA)_2PbI_4$ realized by exploiting its strong interlayer interactions to block ion migration paths. The Br-substituted aromatic spacers not only form strong molecular interactions through Br atoms and neighboring benzene rings (Br···π) but also anchor to inorganic perovskite sheets via strong halogen bonds (Br−I), therefore allowing the ion migration to be suppressed and further enabling highly stable X-ray detectors. Finally, solution-grown high-quality single crystals of $(BPEA)_2PbI_4$ were fabricated into direct X-ray detectors, possessing a high sensitivity of 1003 $\mu C\ Gy^{-1}\ cm^{-2}$ as well as a low baseline drift of 3.48×10^{-8} nA $cm^{-1}\ s^{-1}\ V^{-1}$ at a high 80 V bias. Impressively, this detector also shows exceptional device stability when working under continuous X-ray irradiation and large external electric field as well as exposure to ambient air. This study demonstrates that strengthening interlayer interactions is an effective strategy for stabilizing 2D perovskite X-ray detectors, which sheds light on improving the device stability of perovskite optoelectronics.

METHODS

Synthesis and Crystal Growth

To synthesize $(BPEA)_2PbI_4$, 1 mmol (379 mg) of lead acetate trihydrate ($Pb(Ac)_2{\cdot}3H_2O$, 99.5%) was dissolved in the mixture of 15 mL of hydriodic acid solution (HI, 48 wt % in water) and 0.2 mL of hypophosphorous acid (H_3PO_2, 50 wt % in water) under continuous heating and stirring. Then, 1 mmol (200 mg) of (*R*)-(+)-1-(4-bromophenyl)ethylamine (BPEA, 98%) was added into the solution dropwise. After a transparent yellow solution was obtained, we stopped heating and stirring and let it cool to room temperature, and finally, yellow microcrystals of $(BPEA)_2PbI_4$ were precipitated. Microcrystals of $(MBA)_2PbI_4$ were synthesized by dissolving 1 mmol $Pb(Ac)_2{\cdot}3H_2O$ (379 mg), 1 mmol (*R*)-(+)-α- methylbenzylamine (MBA, 121 mg, 99%) in the mixed solution of HI (10 mL) and H_3PO_2 (0.2 mL). Under continuous heating and stirring, a clear yellow solution was obtained. Then, the heating and stirring were stopped, and the solution was cooled to room temperature. At last, orange needle-like microcrystals were obtained. Bulk single crystals of $(BPEA)_2PbI_4$ and $(MBA)_2PbI_4$ were grown from their saturated solutions, respectively, through a slow temperature cooling process (1 °C per day).

Characterizations

X-ray diffraction patterns were measured on a Miniflex 600 X-ray diffractometer (Rigaku) with Cu Kα radiation. The surface micromorphology and corresponding elemental distribution mappings of single crystals were acquired using a field emission electron microscope (JSM6700-F, JEOL) attached to an energy-dispersive X-ray spectroscope (X-Max^N, Oxford Instrument). The absorption spectrum was recorded on a UV−vis-NIR spectrometer (Lambda 950, PerkinElmer). Thermogravimetric curves were measured on a STA F4 Jupiter simultaneous thermal analyzer (Netzsch) in a N_2 atmosphere from room temperature to 700 °C with a heating speed of 10 °C min^{-1}. The temperature-dependent conductivities of single crystals were derived from their resistance−temperature curves, which were measured using a high-precision electrometer (6517B, Keithley) by placing samples on a heating−cooling stage (THMS600, Linkam).

Device Fabrication and X-ray Detection

A two-terminal Ag/$(BPEA)_2PbI_4$ SC/Ag device structure with Ag deposited on two sides of a single crystal was applied (Figure S12). As one of the typical samples, the size of a single crystal was about 1 × 1 × 0.4 mm^3, the electrode geometry was rectangular with an area of 0.004 cm^2 and the electrode spacing was about 1 mm. The X-ray irradiation was applied on the top of the single-crystal device. *I*−*t* curves of the $(BPEA)_2PbI_4$ single crystal detector under X-ray irradiation were also measured using a Keithley 6517B high-precision electrometer. A commercial X-ray tube (Mini-X2, Amptek) with an Ag target (maximum power: 4W, maximum X-ray photon energy: 50 keV, characteristic X-ray photon energy: 22 keV) was used as the X-ray source. The dose rate was measured by the Accu-Gold X-ray dosimeter (Radcal) with a 10 × 6-180 model ion chamber.

ASSOCIATED CONTENT

Supporting Information

The Supporting Information is available free of charge at https://pubs.acs.org/doi/10.1021/jacsau.4c00345.

Additional experimental information, XRD patterns, TG curve, trap density calculation, molecular interaction analysis, bulk resistivity, device structure and photographs, *I*−*V* and *I*−*t* curves, and X-ray detection performance comparison (PDF)

AUTHOR INFORMATION

Corresponding Authors

Shihai You − *Research Institute of Frontier Science, Southwest Jiaotong University, Chengdu, Sichuan 610031, China;* orcid.org/0000-0002-1537-7148; Email: shihai.you@swjtu.edu.cn

Junhua Luo − *State Key Laboratory of Structural Chemistry, Fujian Institute of Research on the Structure of Matter, Chinese Academy of Sciences, Fuzhou, Fujian 350002, China; Fujian Science and Technology Innovation Laboratory for Optoelectronic Information of China, Fuzhou, Fujian 350108, China; College of Chemistry and Materials Science, Fujian Normal University, Fuzhou, Fujian 350007, China; Key Laboratory of Fluorine and Silicon for Energy Materials and Chemistry of Ministry of Education, School of Chemistry and Chemical Engineering, Jiangxi Normal University, Nanchang, Jiangxi 330022, China;* orcid.org/0000-0002-3179-7652; Email: jhluo@fjirsm.ac.cn

Authors

Haiqing Zhong − *State Key Laboratory of Structural Chemistry, Fujian Institute of Research on the Structure of Matter, Chinese Academy of Sciences, Fuzhou, Fujian 350002, China; College of Chemistry and Materials Science, Fujian Normal University, Fuzhou, Fujian 350007, China*

Jianbo Wu − *State Key Laboratory of Structural Chemistry, Fujian Institute of Research on the Structure of Matter, Chinese Academy of Sciences, Fuzhou, Fujian 350002, China; Fujian Science and Technology Innovation Laboratory for Optoelectronic Information of China, Fuzhou, Fujian 350108, China*

Zeng-Kui Zhu − *State Key Laboratory of Structural Chemistry, Fujian Institute of Research on the Structure of Matter, Chinese Academy of Sciences, Fuzhou, Fujian 350002, China; Fujian Science and Technology Innovation Laboratory for Optoelectronic Information of China, Fuzhou, Fujian 350108, China; Key Laboratory of Fluorine and Silicon for Energy Materials and Chemistry of Ministry of Education, School of Chemistry and Chemical Engineering, Jiangxi Normal University, Nanchang, Jiangxi 330022, China*

Panpan Yu − *Key Laboratory of Fluorine and Silicon for Energy Materials and Chemistry of Ministry of Education, School of Chemistry and Chemical Engineering, Jiangxi Normal University, Nanchang, Jiangxi 330022, China*

Hang Li − *State Key Laboratory of Structural Chemistry, Fujian Institute of Research on the Structure of Matter, Chinese Academy of Sciences, Fuzhou, Fujian 350002, China; Fujian Science and Technology Innovation Laboratory for Optoelectronic Information of China, Fuzhou, Fujian 350108, China*

Zi-Yang Wu − *Kuang Yaming Honors School, Nanjing University, Nanjing, Jiangsu 210023, China*

Yang Li − *Shenzhen Institute of Advanced Technology, Chinese Academy of Sciences, Shenzhen, Guangdong 518055, China*

Qianwen Guan − *State Key Laboratory of Structural Chemistry, Fujian Institute of Research on the Structure of Matter, Chinese Academy of Sciences, Fuzhou, Fujian 350002, China; Fujian Science and Technology Innovation Laboratory for Optoelectronic Information of China, Fuzhou, Fujian 350108, China*

Hongliang Dai − *Key Laboratory of Fluorine and Silicon for Energy Materials and Chemistry of Ministry of Education, School of Chemistry and Chemical Engineering, Jiangxi Normal University, Nanchang, Jiangxi 330022, China*

Chang Qu − *State Key Laboratory of Structural Chemistry, Fujian Institute of Research on the Structure of Matter, Chinese Academy of Sciences, Fuzhou, Fujian 350002, China; College of Chemistry and Materials Science, Fujian Normal University, Fuzhou, Fujian 350007, China*

Jiahong Wang − *Shenzhen Institute of Advanced Technology, Chinese Academy of Sciences, Shenzhen, Guangdong 518055, China;* orcid.org/0000-0002-6743-7923

Shuang Chen − *Kuang Yaming Honors School, Nanjing University, Nanjing, Jiangsu 210023, China;* orcid.org/0000-0003-1334-2213

Chengmin Ji − *State Key Laboratory of Structural Chemistry, Fujian Institute of Research on the Structure of Matter, Chinese Academy of Sciences, Fuzhou, Fujian 350002, China; Fujian Science and Technology Innovation Laboratory for Optoelectronic Information of China, Fuzhou, Fujian 350108, China*

Complete contact information is available at: https://pubs.acs.org/10.1021/jacsau.4c00345

Author Contributions

H.Z.: data curation, formal analysis, investigation, visualization, wiring-original draft; S.Y.: conceptualization, data curation, formal analysis, funding acquisition, methodology, supervision, visualization, writing-review, and editing; J.W.: data curation, formal analysis; Z.-K.Z.: data curation, formal analysis; P.Y.: data curation, formal analysis; H.L.: data curation; Z.-Y.W.: data curation, formal analysis; Y.L.: data curation; Q.G.: data curation; H.D.: data curation; C.Q.: data curation; J.W.: formal analysis, funding acquisition; S.C.: formal analysis, methodology, writing-review, and editing; C.J.: formal analysis, funding acquisition, writing-review, and editing; J.L.: formal analysis, funding acquisition, project administration, supervision, writing-review and editing. All authors have approved the final version of the manuscript. CRediT: **Haiqing Zhong** data curation, formal analysis, investigation, visualization, writing-original draft; **Shihai You** conceptualization, data curation, formal analysis, funding acquisition, methodology, supervision, visualization, writing-review & editing; **Jianbo Wu** data curation, formal analysis; **Zeng-Kui Zhu** data curation, formal analysis; **Panpan Yu** data curation, formal analysis; **Hang Li** data curation; **Zi-Yang Wu** data curation, formal analysis; **Yang Li** data curation; **Qianwen Guan** data curation; **Hongliang Dai** data curation; **Chang Qu** data curation; **Jiahong Wang** formal analysis, funding acquisition; **Shuang Chen** formal analysis, methodology, writing-review & editing; **Chengmin Ji** formal analysis, funding acquisition, writing-review & editing; **Junhua Luo** formal analysis, funding acquisition, project administration, supervision, writing-review & editing.

Notes

The authors declare no competing financial interest.

■ ACKNOWLEDGMENTS

This work is financially supported by the National Natural Science Foundation of China (22193042, 21921001, 22125110, 22122507, U21A2069, 52202194, 21833010, 21971238), the Key Research Program of Frontier Sciences of the Chinese Academy of Sciences (ZDBS-LY-SLH024), the New Interdisciplinary Cultivation Funds of Southwest Jiaotong University (2682024KJ002), the Fundamental Research Funds for the Central Universities (2682024CX098), and the Youth Innovation Promotion of CAS (2020354).

■ REFERENCES

(1) Yaffe, M. J.; Rowlands, J. A. X-ray detectors for digital radiography. *Phys. Med. Biol.* **1997**, *42*, 1−39.

(2) Kasap, S.; Frey, J. B.; Belev, G.; Tousignant, O.; Mani, H.; Greenspan, J.; Laperriere, L.; Bubon, O.; Reznik, A.; DeCrescenzo, G.; Karim, K. S.; Rowlands, J. A. Amorphous and polycrystalline photoconductors for direct conversion flat panel X-ray image sensors. *Sensors* **2011**, *11*, 5112−5157.

(3) Kim, Y. C.; Kim, K. H.; Son, D.-Y.; Jeong, D.-N.; Seo, J.-Y.; Choi, Y. S.; Han, I. T.; Lee, S. Y.; Park, N.-G. Printable organometallic perovskite enables large-area, low-dose X-ray imaging. *Nature* **2017**, *550*, 87−91.

(4) Chen, Q.; Wu, J.; Ou, X.; Huang, B.; Almutlaq, J.; Zhumekenov, A. A.; Guan, X.; Han, S.; Liang, L.; Yi, Z.; Li, J.; Xie, X.; Wang, Y.; Li, Y.; Fan, D.; Teh, D. B. L.; All, A. H.; Mohammed, O. F.; Bakr, O. M.; Wu, T.; Bettinelli, M.; Yang, H.; Huang, W.; Liu, X. All-inorganic perovskite nanocrystal scintillators. *Nature* **2018**, *561*, 88−93.

(5) Li, Z.; Zhou, F.; Yao, H.; Ci, Z.; Yang, Z.; Jin, Z. Halide perovskites for high-performance X-ray detector. *Mater. Today* **2021**, *48*, 155−175.

(6) You, S.; Zhu, Z.-K.; Dai, S.; Wu, J.; Guan, Q.; Zhu, T.; Yu, P.; Chen, C.; Chen, Q.; Luo, J. Inch-size single crystals of lead-fee chiral perovskites with bulk photovoltaic effect for stable self-driven X-ray detection. *Adv. Funct. Mater.* **2023**, *33*, No. 2303523.

(7) Wu, J.; You, S.; Yu, P.; Guan, Q.; Zhu, Z.-K.; Li, Z.; Qu, C.; Zhong, H.; Li, L.; Luo, J. Chirality inducing polar photovoltage in a 2D lead-free double perovskite toward self-powered X-ray detection. *ACS Energy Lett.* **2023**, *8*, 2809−2816.

(8) Pan, W.; Wu, H.; Luo, J.; Deng, Z.; Ge, C.; Chen, C.; Jiang, X.; Yin, W.-J.; Niu, G.; Zhu, L.; Yin, L.; Zhou, Y.; Xie, Q.; Ke, X.; Sui, M.; Tang, J. $Cs_2AgBiBr_6$ single-crystal X-ray detectors with a low detection limit. *Nat. Photonics* **2017**, *11*, 726−732.

(9) Zhuang, R.; Wang, X.; Ma, W.; Wu, Y.; Chen, X.; Tang, L.; Zhu, H.; Liu, J.; Wu, L.; Zhou, W.; Liu, X.; Yang, Y. Highly sensitive X-ray detector made of layered perovskite-like $(NH_4)_3Bi_2I_9$ single crystal with anisotropic response. *Nat. Photonics* **2019**, *13*, 602−608.

(10) Liu, Y.; Xu, Z.; Yang, Z.; Zhang, Y.; Cui, J.; He, Y.; Ye, H.; Zhao, K.; Sun, H.; Lu, R.; Liu, M.; Kanatzidis, M. G.; Liu, S. Inch-size 0D-structured lead-free perovskite single crystals for highly sensitive stable X-ray imaging. *Matter* **2020**, *3*, 180−196.

(11) Dun, G.-H.; Zhang, H.; Qin, K.; Tan, X.; Zhao, R.; Chen, M.; Huang, Y.; Geng, X.-S.; Li, Y.-Y.; Li, Y.; Wan, P.; Gou, G.-Y.; Feng, Q.-X.; Zheng, X.-R.; Liang, R.; Xie, D.; Zhou, Y.; Wang, X.; Tian, H.;

Yang, Y.; Ren, T.-L. Wafer-scale photolithography-pixeled Pb-free perovskite X-ray detectors. *ACS Nano* **2022**, *16*, 10199−10208.
(12) Yakunin, S.; Sytnyk, M.; Kriegner, D.; Shrestha, S.; Richter, M.; Matt, G.; Azimi, H.; Brabec, C.; Stangl, J.; Kovalenko, M.; Heiss, W. Detection of X-ray photons by solution-processed organic-inorganic perovskites. *Nat. Photonics* **2015**, *9*, 444−449.
(13) Wei, H.; Fang, Y.; Mulligan, P.; Chuirazzi, W.; Fang, H.-H.; Wang, C.; Ecker, B. R.; Gao, Y.; Loi, M. A.; Cao, L.; Huang, J. Sensitive X-ray detectors made of methylammonium lead tribromide perovskite single crystals. *Nat. Photonics* **2016**, *10*, 333−339.
(14) Wei, H.; Huang, J. Halide lead perovskites for ionizing radiation detection. *Nat. Commun.* **2019**, *10*, 1066.
(15) Zhou, Y.; Chen, J.; Bakr, O. M.; Mohammed, O. F. Metal halide perovskites for X-ray imaging scintillators and detectors. *ACS Energy Lett.* **2021**, *6*, 739−768.
(16) Jiang, J.; Xiong, M.; Fan, K.; Bao, C.; Xin, D.; Pan, Z.; Fei, L.; Huang, H.; Zhou, L.; Yao, K.; Zheng, X.; Shen, L.; Gao, F. Synergistic strain engineering of perovskite single crystals for highly stable and sensitive X-ray detectors with low-bias imaging and monitoring. *Nat. Photonics* **2022**, *16*, 575−581.
(17) Shrestha, S.; Fischer, R.; Matt, G. J.; Feldner, P.; Michel, T.; Osvet, A.; Levchuk, I.; Merle, B.; Golkar, S.; Chen, H.; Tedde, S. F.; Schmidt, O.; Hock, R.; Rührig, M.; Göken, M.; Heiss, W.; Anton, G.; et al. High-performance direct conversion X-ray detectors based on sintered hybrid lead triiodide perovskite wafers. *Nat. Photonics* **2017**, *11*, 436−440.
(18) Peng, J.; Xu, Y.; Yao, F.; Huang, H.; Li, R.; Lin, Q. Ion-exchange-induced slow crystallization of 2D-3D perovskite thick junctions for X-ray detection and imaging. *Matter* **2022**, *5*, 2251−2264.
(19) Song, Y.; Li, L.; Hao, M.; Bi, W.; Wang, A.; Kang, Y.; Li, H.; Li, X.; Fang, Y.; Yang, D.; Dong, Q. Elimination of interfacial-electrochemical-reaction-induced polarization in perovskite single crystals for ultra-sensitive and stable X-ray detector arrays. *Adv. Mater.* **2021**, *33*, No. 2103078.
(20) Glushkova, A.; Andričević, P.; Smajda, R.; Náfrádi, B.; Kollár, M.; Djokić, V.; Arakcheeva, A.; Forró, L.; Pugin, R.; Horváth, E. Ultrasensitive 3D aerosol-jet-printed perovskite X-ray photodetector. *ACS Nano* **2021**, *15*, 4077−4084.
(21) Wang, Z.; Tie, S.; Zhang, H.; Wan, C.; Liang, Z.; Xu, H.; Zheng, X.; Zhang, W.; Aldakov, D.; Reiss, P.; Ye, J.; Pan, X. Supple formamidinium-based low-dimension perovskite derivative for sensitive and ultrastable X-ray detection. *ACS Nano* **2023**, *17*, 13638−13647.
(22) Xu, X.; Qian, W.; Xiao, S.; Wang, J.; Zheng, S.; Yang, S. Halide perovskites: a dark horse for direct X-ray imaging. *EcoMat* **2020**, *2*, No. e12064.
(23) Lin, Y.; Bai, Y.; Fang, Y.; Wang, Q.; Deng, Y.; Huang, J. Suppressed ion migration in low-dimensional perovskites. *ACS Energy Lett.* **2017**, *2*, 1571−1572.
(24) Saidaminov, M. I.; Mohammed, O. F.; Bakr, O. M. Low-dimensional-networked metal halide perovskites: the next big thing. *ACS Energy Lett.* **2017**, *2*, 889−896.
(25) Tsai, H.; Liu, F.; Shrestha, S.; Fernando, K.; Tretiak, S.; Scott, B.; Vo, D. T.; Strzalka, J.; Nie, W. A sensitive and robust thin-film x-ray detector using 2D layered perovskite diodes. *Sci. Adv.* **2020**, *6*, No. eaay0815.
(26) Yukta; Ghosh, J.; Afroz, M. A.; Alghamdi, S.; Sellin, P. J.; Satapathi, S. Efficient and highly stable X-ray detection and imaging using 2D $(BA)_2PbI_4$ perovskite single crystals. *ACS Photon.* **2022**, *9*, 3529−3539.
(27) You, S.; Yu, P.; Wu, J.; Zhu, Z.-K.; Guan, Q.; Li, L.; Ji, C.; Liu, X.; Luo, J. Weak X-ray to visible lights detection enabled by a 2D multilayered lead iodide perovskite with iodine-substituted spacer. *Adv. Sci.* **2023**, *10*, No. 2301149.
(28) Ren, H.; Yu, S.; Chao, L.; Xia, Y.; Sun, Y.; Zuo, S.; Li, F.; Niu, T.; Yang, Y.; Ju, H.; Li, B.; Du, H.; Gao, X.; Zhang, J.; Wang, J.; Zhang, L.; Chen, Y.; Huang, W. Efficient and stable Ruddlesden-Popper perovskite solar cell with tailored interlayer molecular interaction. *Nat. Photonics* **2020**, *14*, 154−163.
(29) Fu, X.; Wang, M.; Jiang, Y.; Guo, X.; Zhao, X.; Sun, C.; Zhang, L.; Wei, K.; Hsu, H.-Y.; Yuan, M. Mixed-halide perovskites with halogen bond induced interlayer locking structure for stable pure-red PeLEDs. *Nano Lett.* **2023**, *23*, 6465−6473.
(30) Zhang, B.; Xu, Z.; Ma, C.; Li, H.; Liu, Y.; Gao, L.; Zhang, J.; You, J.; Liu, S. First-principles calculation design for 2D perovskite to suppress ion migration for high-performance X-ray detection. *Adv. Funct. Mater.* **2022**, *32*, No. 2110392.
(31) Zhang, B.; Zheng, T.; You, J.; Ma, C.; Liu, Y.; Zhang, L.; Xi, J.; Dong, G.; Liu, M.; Liu, S. Electron-phonon coupling suppression by enhanced lattice rigidity in 2D perovskite single crystals for high-performance X-ray detection. *Adv. Mater.* **2023**, *35*, No. 2208875.
(32) Li, H.; Song, J.; Pan, W.; Xu, D.; Zhu, W.; Wei, H.; Yang, B. Sensitive and stable 2D perovskite single-crystal X-ray detectors enabled by a supramolecular anchor. *Adv. Mater.* **2020**, *32*, No. 2003790.
(33) Song, J.; Feng, X.; Wei, H.; Yang, B. Supramolecular interactions of flexible 2D perovskite in microstrain releasing and optoelectronic properties recovery. *Adv. Funct. Mater.* **2022**, *32*, No. 2203329.
(34) Li, W.; Feng, X.; Guo, K.; Pan, W.; Li, M.; Liu, L.; Song, J.; He, Y.; Wei, H. Prominent free charges tunneling through organic interlayer of 2D perovskites. *Adv. Mater.* **2023**, *35*, No. 2211808.
(35) Peng, Y.; Liu, X.; Li, L.; Yao, Y.; Ye, H.; Shang, X.; Chen, X.; Luo, J. Realization of *vis*-NIR dual-modal circularly polarized light detection in chiral perovskite bulk crystals. *J. Am. Chem. Soc.* **2021**, *143*, 14077−14082.
(36) Guan, Q.; Zhu, T.; Zhu, Z.-K.; Ye, H.; You, S.; Xu, P.; Wu, J.; Niu, X.; Zhang, C.; Liu, X.; Luo, J. Unprecedented chiral three-dimensional hybrid organic-inorganic perovskitoids. *Angew. Chem., Int. Ed.* **2023**, *62*, No. e202307034.
(37) Spackman, P. R.; Turner, M. J.; McKinnon, J. J.; Wolff, S. K.; Grimwood, D. J.; Jayatilaka, D.; Spackman, M. A. CrystalExplorer: a program for Hirshfeld surface analysis, visualization and quantitative analysis of molecular crystals. *J. Appl. Crystallogr.* **2021**, *54*, 1006−1011.
(38) Lu, P.; Li, T.; Lu, M.; Ruan, C.; Sun, S.; Wu, Z.; Zhong, Y.; Zhang, F.; Gao, Y.; Huang, Y.; Wang, Y.; Hu, J.; Yan, F.; Zhang, Y. Enrichment of anchoring sites by introducing supramolecular halogen bonds for the efficient perovskite nanocrystal LEDs. *Light: Sci. Appl.* **2023**, *12*, 215.
(39) Zhang, Y.; Liu, Y.; Xu, Z.; Yang, Z.; Liu, S. 2D perovskite single crystals with suppressed ion migration for high-performance planar-type photodetectors. *Small* **2020**, *16*, No. 2003145.
(40) Yang, S.; Chen, S.; Mosconi, E.; Fang, Y.; Xiao, X.; Wang, C.; Zhou, Y.; Yu, Z.; Zhao, J.; Gao, Y.; Angelis, F. D.; Huang, J. Stabilizing halide perovskite surfaces for solar cell operation with wide-bandgap lead oxysalts. *Science* **2019**, *365*, 473−478.
(41) Tauc, J. Optical properties and electronic structure of amorphous Ge and Si. *Mater. Res. Bull.* **1968**, *3*, 37−46.
(42) Xu, Z.; Liu, X.; Li, Y.; Liu, X.; Yang, T.; Ji, C.; Han, S.; Xu, Y.; Luo, J.; Sun, Z. Exploring lead-free hybrid double perovskite crystals of $(BA)_2CsAgBiBr_7$ with large mobility-lifetime product toward X-ray detection. *Angew. Chem., Int. Ed.* **2019**, *58*, 15757−15761.
(43) Han, S.; Yao, Y.; Liu, X.; Li, B.; Ji, C.; Sun, Z.; Hong, M.; Luo, J. Highly oriented thin films of 2D Ruddlesden-Popper hybrid perovskite toward superfast response photodetectors. *Small* **2019**, *15*, No. 1901194.
(44) Ji, D.; Li, T.; Liu, J.; Amirjalayer, S.; Zhong, M.; Zhang, Z.-Y.; Huang, X.; Wei, Z.; Dong, H.; Hu, W.; Fuchs, H. Band-like transport in small-molecule thin films toward high mobility and ultrahigh detectivity phototransistor arrays. *Nat. Commun.* **2019**, *10*, 12.
(45) Fang, F.; Wan, Y.; Li, H.; Fang, S.; Huang, F.; Zhou, B.; Jiang, K.; Tung, V.; Li, L.-J.; Shi, Y. Two-dimensional $Cs_2AgBiBr_6/WS_2$ heterostructure-based photodetector with boosted detectivity via interfacial engineering. *ACS Nano* **2022**, *16*, 3985−3993.

https://doi.org/10.1021/jacsau.4c00345
JACS Au 2024, 4, 2393−2402

(46) Tu, Y.; Xu, Y.; Li, J.; Hao, Q.; Liu, X.; Qi, D.; Bao, C.; He, T.; Gao, F.; Zhang, W. Ultrathin single-crystalline 2D perovskite photoconductor for high-performance narrowband and wide linear dynamic range photodetection. *Small* **2020**, *16*, No. 2005626.
(47) NIST Physical Measurement Laboratory. X-ray form factor, attenuation, and scattering tables. https://www.nist.gov./pml/x-ray-form-factor-attenuation-and-scattering-tables (accessed Apr, 2024).
(48) Liu, W.; Shi, T.; Zhu, J.; Zhang, Z.; Li, D.; He, X.; Fan, X.; Meng, L.; Wang, J.; He, R.; Ge, Y.; Liu, Y.; Chu, P. K.; Yu, X.-F. PbI_2-DMSO assisted in situ growth of perovskite wafers for sensitive direct X-ray detection. *Adv. Sci.* **2023**, *10*, No. 2204512.

https://doi.org/10.1021/jacsau.4c00345
JACS Au 2024, 4, 2393−2402